X-ray tomography crystal characterization: Growth monitoring

Gautier Hypolite, Jérôme Vicente, Hugo Taligrot, Philippe Moulin

X-ray tomography crystal characterization: Growth monitoring

Gautier Hypolite [a], Jérôme Vicente [b], Hugo Taligrot [a], Philippe Moulin [a,*]

[a] Aix Marseille Univ., CNRS, Centrale Marseille, (M2P2 UMR 7340), Equipe Procédés Membranaires (EPM), Europôle de l'Arbois, BP80, Pavillon Laennec, Hall C, 13545 Aix en Provence cedex, France
[b] Aix Marseille Univ., Institut Universitaire des Systèmes Thermiques Industriels (IUSTI-CNRS-UMR 6595), Technopôle de Château-Gombert, 5 rue Enrico Fermi, 13453 Marseille cedex 13, France

ARTICLE INFO

Communicated by Alexander Van Driessche

Keywords:
A1. X-ray tomography
A1. Crystal characterization
A1. Growth monitoring, C. segmentation

ABSTRACT

In this study, we present a new approach for the growth monitoring of crystals using micro X-ray computed tomography (XCT). This technique allows us to track the evolution of the total crystal volume and surface in real time, and to calculate the growth rate. By segmenting the 3D XCT images using a robust method, we are able to extract detailed information about the crystals, such as their number, volume, diameter, and sphericity. Additionally, we determine the growth rates of individual crystal faces. Our method has the potential to greatly benefit the pharmaceutical and chemical industries, as it provides insight into the structural parameters of crystals during growth, which is crucial for optimization and control.

1. Introduction

Control of crystals' structural parameters during growth is essential, for example for the pharmaceutical and chemical industries. Indeed, the crystal growth process can impact the final compound properties [1], such as the purity, the crystals sizes distribution, the crystal faces and polymorphism [2], or the crystals stability. By determining the final shape of the crystals, the growth process influences the solubility, compatibility, and flowability of bulk powders [3]. All of this can impact product uniformity, dissolution, or bioavailability and therefore impact the safety and efficacy of the drugs [4]. Ma et al. [5] provide a comprehensive review of recent advancements in crystal morphology research, including crystal shape distribution modeling, measurement and estimation of crystal facet growth kinetics, and 3D imaging for characterization of crystal morphology and shape distribution. Different experimental techniques are used for crystal growth rate measurements. Most of the methods are focused on a single crystal, to determined individual face growth rates. For example, Wu et al. [6] have developed an instrument that allows the measurement of face-specific growth kinetics of crystals. Using 3D online imaging, this instrument can accurately obtain growth rates for all independent crystal faces. The resulting growth kinetic models can then be integrated into simulations to predict the evolution of crystal shapes. In addition to single crystal growth, measurements on populations of crystals are useful to understand size-dependent growth and are therefore useful for process control [1]. De Anda et al. [7] present a method, based on 2D images for the measurement of crystal facet growth rates on a population. Direct measurement of crystal volume and surface area can also be performed using X-ray computed tomography [4,8,9]. X-ray computed tomography (XCT) is a non-destructive imaging technique that allows reconstructing 3D images of a sample. The 3D images are obtained from multiple radiographic projections of the sample for a complete rotation [10]. The X-rays passing through the sample are attenuated [11] and mark the detector to form an X-ray projection. The greyscale X-ray image obtained at the detector is then recorded. Based on all these projections, a back-projection algorithm is used to provide volume density information (3D reconstruction) [12], where the grey levels of the reconstructed image reflect a local density. We can then access the differences in composition and the presence of heterogeneities (pores, inclusions, etc.) within the sample. XCT has been used to study packing structures and determine topological quantities (size, distribution, contact numbers, contact angle distributions, and even contact surfaces) [13]. In the pharmaceutical industry, XCT has been used for crystal powder studying, for example, to characterize crystals powder microstructure [8] or to measure the particle packing of pharmaceutical design [4]. In these works [4,8], XCT images are analyzed using a conventional watershed particle segmentation algorithm [14,15]. These analyses allow them to describe the volume, shape, and size distribution of particles in the crystal powder. Kovačevic et al. [16] used XCT for crystal analysis and proposed a novel approach that combines the Hough transform for

* Corresponding author.
E-mail address: philippe.moulin@univ-amu.fr (P. Moulin).

crystal face recognition with a parametrized representation of crystal shape. Their algorithm offers an efficient way to identify the parameters of a crystal shape, enabling the identification of faceted crystal shapes, even in the presence of imperfect or broken crystals. In their study, the authors demonstrated the effectiveness of their approach on a set of potash alum crystals, which included both highly regular and imperfect crystals. They suggest that the technique can be automated to extract the full particle size-and-shape distribution, making it a valuable tool for particle characterization. Hypolite et al. [9] also proposed an automatic crystal recognition method based on XCT 3D images. The method aims to increase the accuracy of crystal detection compared to classical methods by detecting the crystals flat faces. Unlike Kovačevic et al. [16] who uses Hough transform, they use a surface growing method for face detection.

The aim of this work is to evaluate the possibility of monitoring crystals growth using XCT and use an automatic crystal segmentation to monitor the growth and shape of each crystal by image analysis. The challenge is to achieve sufficiently short acquisition times to characterize the crystals at a precise time while maintaining sufficient image quality for analysis. The crystal growth of two different chemical species formed under different crystallization conditions were studied. Potassium alum (potassium aluminum sulfate dodecahydrate – $K(SO_2)_2$ 12 (H_2O), $Al(SO_2)_2$ 12(H_2O)) and chromium alum (potassium chromium sulfate dodecahydrate – $Cr(SO_2)_2$ 12(H_2O), $Al(SO_2)_2$ 12(H_2O)) are chosen for these experiments as they are readily available and present different crystals shapes.

2. Materials and methods

2.1. Chemicals and preparation

Two chemical species have been chosen for the experiment, and solutions have been made with them. (i) a solution of potassium alum (double sulfate of potassium and aluminum dodecahydrate, 99.5 % purity, Fisher-scientific) with a concentration of 600 g L^{-1} of water initially at 60 °C. (ii) A saturated solution of chromium alum (double sulfate of potassium and chromium dodecahydrate, 99 % purity, Fisher-scientific) at 57 °C. Distilled water was used for solution preparation. The solutions are placed in a test tube (Fig. 1b) in which three cotton yarns have been installed for crystals to grow on them and prevent crystals from falling to the bottom of the tube. Fig. 1a presents a scheme of the test tubes that have been used for the experiment. An example of sample in the final state is presented in Fig. 1b.

When the solution is ready, the test tube is placed in the XCT apparatus. A second tube is prepared in the same way at the same time and is used to measure temperature. In the XCT apparatus the solution temperature decreases until it reaches room temperature. As the solution cools, its saturation increases and crystals form when the solution is supersaturated.

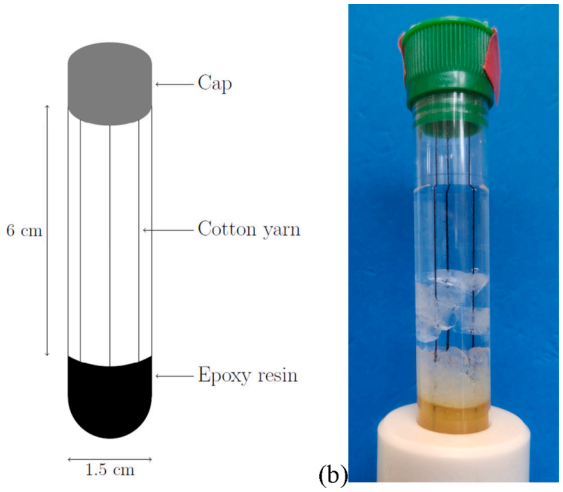

Fig. 1. Test tube used for XCT: (a) Diagram of the test tube with the three cotton yarns; (b) photo of a crystalized potassium alum sample.

For the first (potassium alum) solution, 27 acquisitions were performed from the beginning of the crystallization (t_0) to $t_0 + 75$ *min*. For the second solution (chromium alum), 25 acquisitions were performed from the beginning (t_0) to $t_0 + 51$ *min*. The first acquisition is initiated when the crystallization begins. The beginning of the crystallization can be observed on the live X-ray image.

2.2. X-ray computed tomography

Micro-CT scans were performed with an EasyTomXL150 "Mechanic Ultra" microtomograph (RX-Solution France). An X-ray attenuation higher than the liquid region characterizes the crystals due to their structure. The objective is to obtain the best image quality/acquisition speed ratio. A first study is performed to fix the acquisition parameters. We are looking for the fastest acquisition with sufficient image quality. The image must allow the detection of solid voxels and the identification of crystals. The maximum acquisition speed of the imager is 30 images per second with a scan performed at 114 kV and 208 mA. A binning of 2 is used to increase the luminous flux and thus the contrast in the projections. The binning is done at the expense of the voxel size: the obtained voxel size is 27 μm. For this voxel size, the optimal number of radiographic projections is 544, which corresponds to an angle step between successive projections of 0.66°. These parameters allow the acquisition of the entire interior of the test tube (diameter 14.6 mm on a height of 22.1 mm). To increase the signal-to-noise ratio, each tomographic projection is obtained by means of 3 successive images for the same angular position. This allows to obtain low-noise images with a small impact on the total acquisition time. The final acquisition time is of the order of one minute instead of 20 s with noisier images. This acquisition time is small enough compared to the crystal growth process which takes approximately one hour to complete. The region of interest (ROI) was 541*541*821 voxels (x*y*z). The obtained 3D volume consists of voxels characterized by their Gray Scale Value (GSV) ranging from 0 to 65,535 for a 16-bit image, depending on the X-ray attenuation by the sample. An increase in the GSV corresponds to higher X-ray attenuation. The 16-bit images are converted to 8-bit images characterized by a GSV ranging from 0 to 256. Afterward, the greyscale images are converted to binary images representing the liquid and solid (crystal) phases. The conversion is done by applying a noise filtering process, followed by a threshold operation. Noise filtering is done by applying a non-local mean denoising filter with a sigma value of 7 and a smoothing factor of 1. The *iso*-density threshold allows the separation of the solid phase (crystals) from the fluid phase used for the binarization of volumes is obtained using the Shanbhag method [17]. The method provides a binary 3D image made of voxels. The solid surface is meshed using the marching cubes algorithm [18] with the same threshold value that has been used to separate the solid and liquid phases.

2.3. Image analysis

3D images obtained with XCT are processed to compute crystals volume and surface as well as mean equivalent diameter and sphericity. Crystals volume (V) is the total volume of the solid phase. It is computed as the number of solid phase voxels multiply by the volume of a voxel. Tracking the total crystal volume allows measuring the rate of crystal production (dV/dt) and the overall crystal growth rate. The overall crystal growth rate, which is defined as the mass deposited per unit area per unit time [19], is computed from Eq. (1) with S the total crystal surface. The total surface is approximated by the sum of the surface of the mesh faces.

$$G(t) = \frac{1}{S}\cdot\frac{dV}{dt} \tag{1}$$

In addition to the crystal total volume and surface area, the equivalent diameter (D_e) is used to describe particle size. It is defined as the diameter of the sphere having the same volume as the particle (Eq. (2).

$$D_e = 2\cdot\left(\frac{3}{4}\cdot\frac{V_p}{\pi}\right)^{\frac{1}{3}} \tag{2}$$

With V_p the particle volume (m^3). For practical applications, it can be easier to use the characteristic equivalent diameter D_n than the complete distributions: such a metric corresponds to the cell diameter for which n % of the volume distribution has smaller cell sizes and (100-n)% has larger cell sizes [20]. The equivalent diameter gives information about particle sizes but does not describe the particles' shape. Gajjar et al. [8] suggest to using another metric to describe the shape: the particles' sphericity. Sphericity (S) describes the proximity between an object's shape and a sphere. It is defined as the ratio between the surface of a sphere of the same volume as the object and the surface of the object (A_p) (Eq. (3)). As for the diameter, the characteristic equivalent sphericity S_n is computed.

$$S = \frac{\pi^{\frac{1}{3}}(6V_p)^{\frac{2}{3}}}{A_p} \tag{3}$$

Equivalent diameter and sphericity calculation requires the segmentation of crystals to determine the individual crystals. The segmentation is performed using the crystal segmentation algorithm from [9].

3. Results and discussion

3.1. Image analysis

The image analysis method from Hypolite et al. [9] have been applied on the tomographic images. The final acquisition of the chromium alum sample (after 50 acquisitions) is chosen to illustrate the image analysis method as it presents the largest number of crystals. Fig. 2a present the binary 3D image of the sample obtained by thresholding the original grayscale image. The Münch et al. algorithm [21] is applied to this image (Fig. 2b) as well as the crystal segmentation algorithm [9] (Fig. 2c). The number of particles and shape parameter are described in Table 1.

The validation of the segmentation is a difficult task, for which human eyes are an effective tool. For example, the circled areas on Fig. 2 correspond to particles over-segmented by the Münch algorithm that have been merged by the crystal segmentation algorithm, allowing a better representation of the crystals.

Table 1
Number of particles and particles shape parameter obtained with the Münch et al. and the crystal segmentation algorithm.

Algorithm	Münch	Crystal segmentation
Number of particles	1884	1481
D10 (mm)	0.63	0.68
D50 (mm)	1.11	1.26
D90 (mm)	1.49	1.63
Mean sphericity	0.53	0.53

Table 1 shows that the crystal segmentation algorithm reduces the number of particles by 21% and increases the median particle size by 13.5 % for the same sphericity. The benefit of the crystal segmentation algorithm is to prevent over-segmentation by merging some of the particles recognized by the Münch et al. algorithm based on the crystal flat surfaces. The difference between the crystals' size obtained with the two algorithms show the importance of using an algorithm allowing a correct segmentation. The ability of the crystal segmentation algorithm to correctly segment crystals is detailed by Hypolite et al. [9].

3.2. Crystals growth

Tomographic images are acquired during crystallization of the two samples (potassium alum and chromium alum). Crystallization is obtained by cooling the solution in the ambient air. Tomography acquisitions were made on average every 3 min, with an acquisition time of one minute. For potassium alum, crystallization process was followed during 75 min; 27 acquisitions were performed during the crystallization process. For chromium alum, the crystallization process was followed during 50 min; 25 images were acquired. A part of these images are presented in Table 2. The images show the back half of the test tube, in which two of the three cotton yarns are located. It can first be noticed that despite the short acquisition time it is possible to obtain clear images. Then, using these images, the crystal formation kinetic can be analyzed. Crystals are formed starting from nuclei and grow until they reach their final size. At the beginning, crystals form on the tube wall and on the yarns. Crystals growing on yarns are firmly anchored while those growing on the walls may fall on the bottom when they reach a critical size. The region of interest is situated just above the bottom,

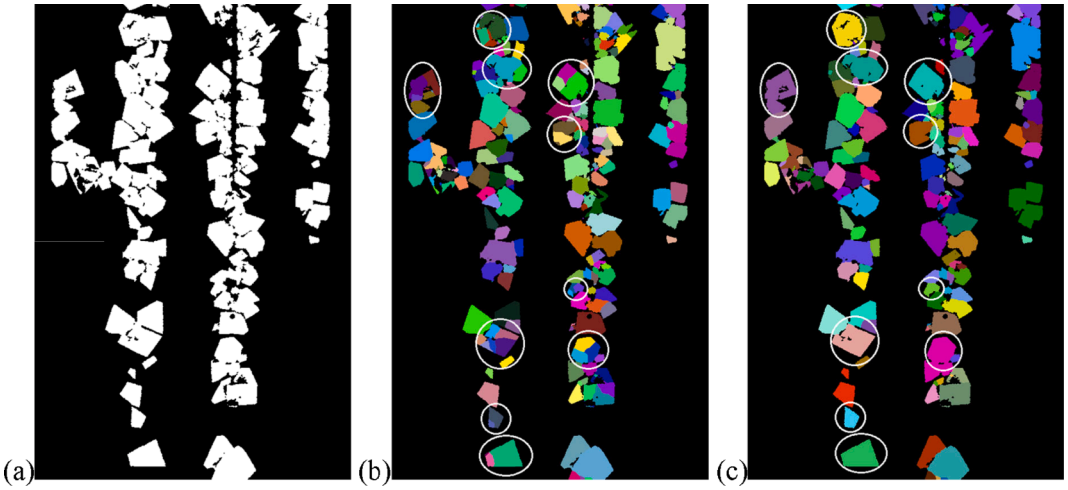

Fig. 2. Image of the chromium sample at the end of the crystallization, transversal cut; (a) binary image, (b) image segmented with Münch et al algorithm; (c) image segmented with crystal segmentation algorithm. The circled areas on Fig. 2 correspond to particles over-segmented by the Münch algorithm that have been merged by the crystal segmentation algorithm.

Table 2
XCT 3D images of chromium alum crystal during crystallization process. Only the back half of the test tube presented.

$t = t_0$; $T = 56°C$	$t = t_0 + 1.5\ min$; $T = 55°C$	$t = t_0 + 4\ min$; $T = 50°C$
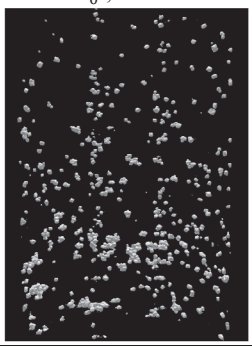	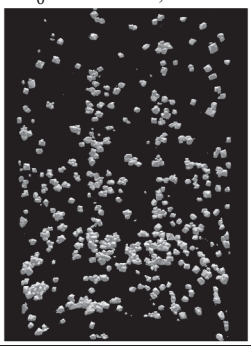	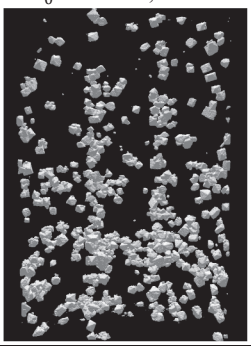
$t = t_0 + 7\ min$; $T = 46°C$	$t = t_0 + 9\ min$; $T = 44°C$	$t = t_0 + 12\ min$; $T = 40°C$
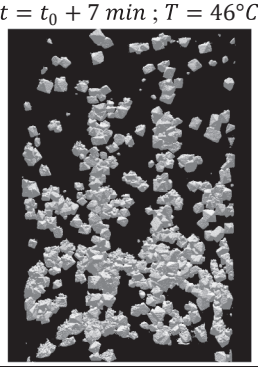	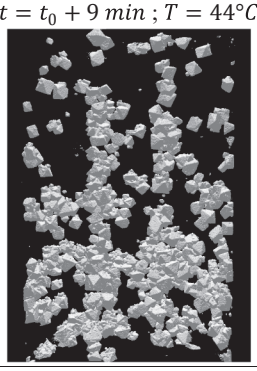	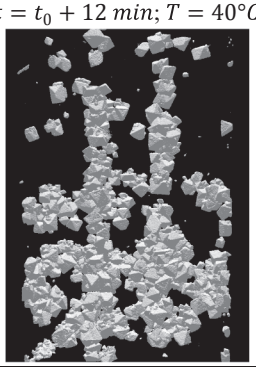
$t = t_0 + 19.5\ min$; $T = 33°C$	$t = t_0 + 29.5\ min$; $T = 28°C$	$t = t_0 + 52\ min$; $T = 22°C$
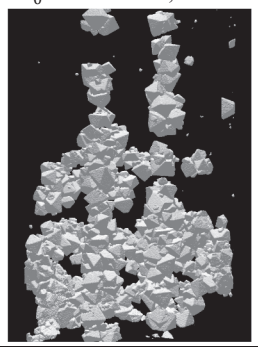	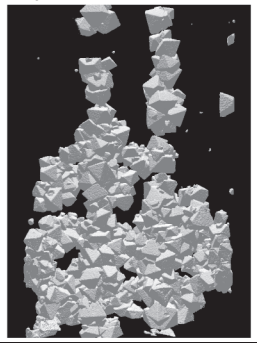	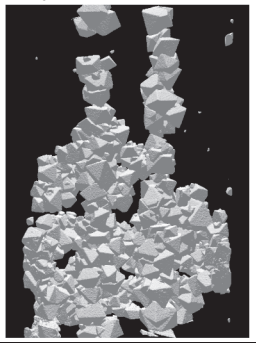

therefore part of the falling crystals gets out of the region of interest.

The rest piles up at the bottom of the region of interest. The falling phenomenon can well be observed between t_0 +12 min and t_0 + 19.5 min. The volume of crystal in the solution according to time and the variation of solution temperature is presented in Fig. 3 for the chromium and potassium alum samples. The time on the abscissa corresponds to the time elapsed since the start of crystallization. Each tomographic acquisition time last 60 secondes. Each point on Fig. 3 represents respectively volume (%), specific surface (mm^{-1}) and surface grow rate ($m\ s^{-1}$) computed for all the crystals of the entire reactor at a specific tomographic acquisition. On the chromium alum volume curve of Fig. 3 (square points in the first graph), it can be observed that two points deviate from the curve at $t_0 + 18$ min and $t_0 + 30$ min. This diminution of crystals volume corresponds to crystals that fall out the region of interest. The acquisitions started for the two samples at the beginning of the crystallization which appeared at the temperatures of 56 °C and 44 °C for the chromium alum and potassium samples respectively. The temperature of the reactor decreases over time and stabilizes around the ambient temperature approximatively after 30 min. While the volume of crystals increases over time in three phases: (i) the first seconds represent the generation of crystals (nucleation phase); (ii) after, the temperature drops rapidly, and the magnification of the crystals accelerates (phase 2); (iii) then, the crystallization slows down until crystallization end (phase 3).

The transition between phases 2 and 3 correspond to the inflection point that can be seen in the volume variations of Fig. 3 (at approximately t_0 +10 min for chromium alum and $t_0 + 35$ min for potassium alum). The rate of crystal production is influenced by two factors: (i) it increases when temperature drops (due to the increase of supersaturation); (ii) it decreases with the specific surface (as the diffusion at the solid/ liquid interface drives the crystal formation). The evolution of specific surface (total volume divided by the crystals surface) according to time is plotted in the second graph of Fig. 3. The specific surface decreases when the crystal grows, therefore, it decreases with time. In phase 2, the production of crystal increases due to temperature drop, in phase 3 crystal growth is limited by the specific surface and the rate of crystal production decreases.

3.3. *Crystal growth rate*

The overall crystal growth rate depends on temperature, supersaturation, or size [19]. The value of the crystal growth rate has been computed with Eq. (1) and plotted on the third graph of Fig. 3 for the two crystallization experiments. The crystal growth rate is plotted as a

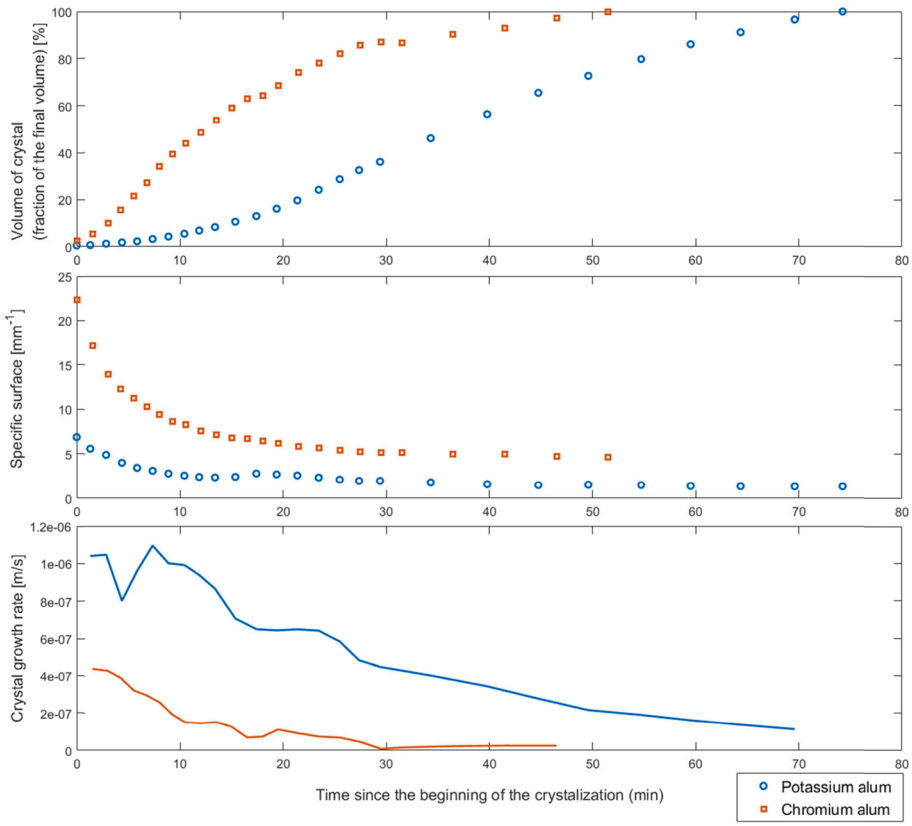

Fig. 3. Volume of crystal, specific surface and crystal growth rate over time during the crystallization process.

continuous line as it is computed using a derivative on the measurement data. Crystals that drop out of the region of interest lead the value below the global trend. For example, at $t_0 + 5$ min in the potassium alum series. The value at $t_0 + 18$ min and $t_0 + 30$ min that we had observed on the chromium alum volume can also be observed here. The crystal growth rate decreases with time down to zero as the temperature decreases.

3.4. *Crystals number*

The segmentation algorithm has been applied to the tomographic

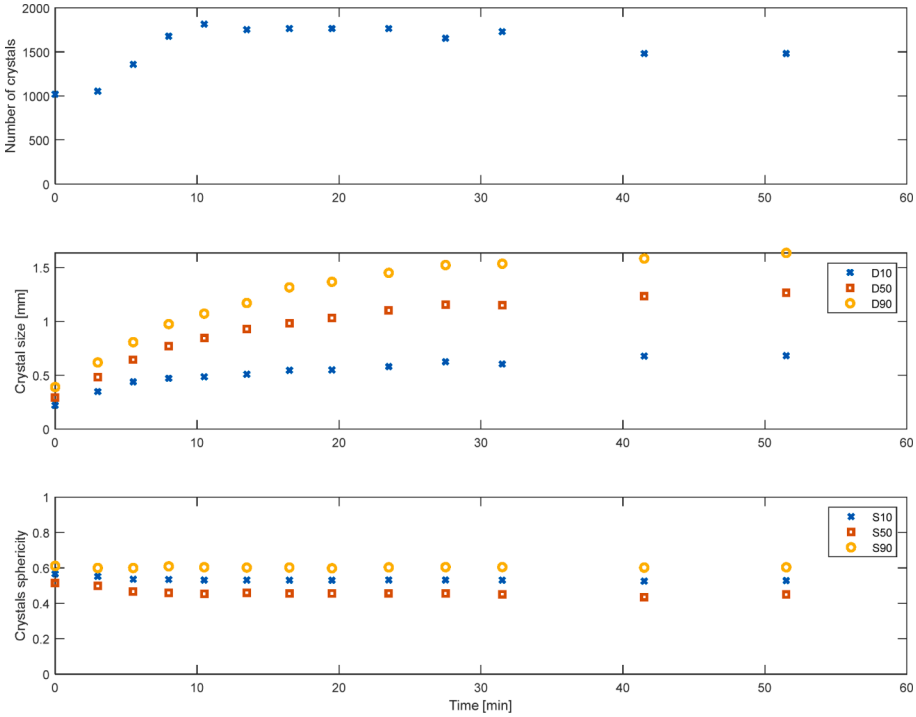

Fig. 4. Evolution of the crystal number, size (D10; D50 and D90) and sphericity (S10; S50 and S90) according to time [Chromium alum, $T_{initial} = 56$ °C].

images of the two samples. The results are presented for the chromium alum sample as it formed a large number of crystals (~1500), while the potassium alum sample forms only three distinct crystals. The final state of crystallization colored according to the segmentation is presented in Fig. 2c. The potassium alum sample crystallized to form a small number of large crystals when the chromium alum sample forms a large number of small crystals. The study of the phenomena influencing the number and size of crystals is not the objective of this study. However, among the phenomena which can explain this result, we can mention: the concentration and the temperature of the initial solution, the degree of supersaturation reached, the presence of nucleation site. The evolution of the crystals number, size and sphericity is presented on Fig. 4. The initial number of crystal correspond to the number of visible crystal on the first tomography i.e. at $t_0 + 1$ min. The small variation of the particle number between the first two tomographies is due to the inability of the crystal segmentation algorithm to correctly segment too small crystal. Indeed the mean particle size at this stage is 290 μm, which correspond to 10 voxels. Therefore, the flat faces cannot be identified at this stage.

The number of crystals is 1019. This high number shows that the main nucleation phase has already taken place. The majority of the crystal's nuclei are created in a few seconds and cannot be captured with XCT. However, during the first phase of the crystallization process, the number of crystals continues to increase, it corresponds to the ending of the crystallization. After approximately 10 min, the number of crystals stabilized and stayed almost constant until the end at 1648 $\pm$ 10%. The slight decrease in the number of crystals during the last phase corresponds to the merge of some crystals during the growth. The crystal size (Fig. 4) increases quickly during the first minutes of the process (growth phase) and stabilized at the end. The evolution of the D50 and D90 equivalent diameter follow the same trend: the D90 value is 30% larger than the D50 value. The D10 value also follows the same trend at the beginning but increase more slowly after $t_0 +$ 5 *min* 30 *s*. This implies that a part of the crystal cannot grow freely, probably because of the proximity with other crystals or with the wall. Overall, the D10, D50 and D90 are similar, which reflects a tight distribution of the crystals' size. The crystal sphericity (Fig. 4) stays constant during the process with a narrow distribution. This is consistent with the growth of crystals maintaining the same shape.

3.5. Growth study of an isolated crystal

A crystal has been isolated, and its growth has been followed on several tomographies. The crystal is isolated based on its position. Fig. 5 shows the evolution of a single crystal slice of potassium alum. Potassium alum is chosen here, as it forms large crystals whose growth is easier to follow than chromium alum crystals. Each line in Fig. 5 corresponds to the crystal outlines on a tomographic acquisition. The crystal grows from the four faces of the nuclei. At some time, a new face is formed at the right of the image, this new face is due to the contact between the crystal and the tube wall. The faces growth rate can be determined from the images; however, the growth will depend on the angle between the face and the cutting plans. The growth rate $G(t_j)$ ($m\ s^{-1}$) of the face i at time t_j is given by (Eq. (4)).

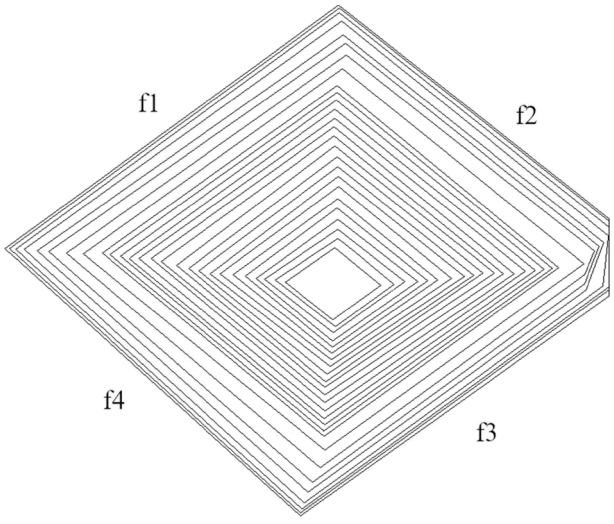

Fig. 5. Evolution of the potassium alum crystal: cross-section view (x = 0). Each line represents the outlines of the crystal on a tomographic acquisition [Potassium alum, $T_{initial} = 44$ °C].

$$G(t_j) = \frac{|\cos(\alpha) \cdot d_i(t_j)|}{t_j - t_{j-1}} \tag{4}$$

With $d_i(t_j)$ the distance (m) between the lines on the cutting plane representing the crystal face at $t = t_{j-1}$ and $t = t_j$; α_i the angle between the cutting plane and the face. The angles are $\alpha_1 = 1.84\ rad$; $\alpha_2 = 1.80\ rad$; $\alpha_3 = 1.84\ rad$; $\alpha_4 = 1.77\ rad$.

First, it can be noticed that the crystal of Fig. 3 grows by approaching a rhombus, which is characteristic for an octahedron slice (the typical form of potassium alum crystal). Then, the evolution of faces growth rate is computed based on Fig. 3 and print in the graph of Fig. 6. In addition, the graph of Fig. 6 shows the global crystal growth rate (same as in Fig. 2).

The faces growth rate is of the same order of magnitude for the four faces. The values are slightly higher than the global growth rate. This can be explained by the presence of a large cluster of crystals at the bottom of the sample, which grows more slowly than this crystal, and then decreases the global growth rate.

4. Conclusion

The temporal evolution of crystal formation, from a cooling solution, has been studied with XCT. Images are processed according to their grayscale value and a crystal segmentation algorithm is applied. Despite the small acquisition time allowed by the process kinetic, the obtained XCT images are sufficiently clear to be analyzed. The method that has been developed allows to determine the temporal evolution of crystal volume, surface, production, and growth rate. The solution temperature is also measured. The crystal segmentation performed on the XCT images allows following the number and shape of the crystals. In addition to these values, the evolution of solution concentration and supersaturation could be determined with a mass balance of the two phases if the region of interest covers the entire volume of solution. The growth rate of specifics face has also been computed and requires the value of the angle between the face and the cutting plane. This type of analysis can be performed on a single crystal as well as on the whole. For the analyzed crystal, the faces growth rate is of the same order of magnitude as the global growth rate and this value is in accordance with the value that can be found in the literature. The method presented in this study is currently limited to laboratory-scale applications. The crystal growth process requires 3D X-ray micro-tomographic image acquisition. As a result, this method cannot be applied to larger crystallizers. Additionally, the sample rotates during acquisition in the tomograph used in this study, which would require the ability to rotate the crystallizer during acquisition to apply this method to industrial processes. Nevertheless, this method can be applied to other crystallizer geometries or different compounds. Indeed, the method has been successfully applied to two species: potassium and chromium alum, but it can be adapted for other compounds that crystallize from solute with a different crystal structure. To use this method, the analyzed compound must gather specific criteria, including: (i) exhibiting different X-ray absorption between the solid and liquid phase; (ii) forming crystals larger than the voxel size; and (iii) having a crystallization time significantly longer than the tomographic acquisition time.

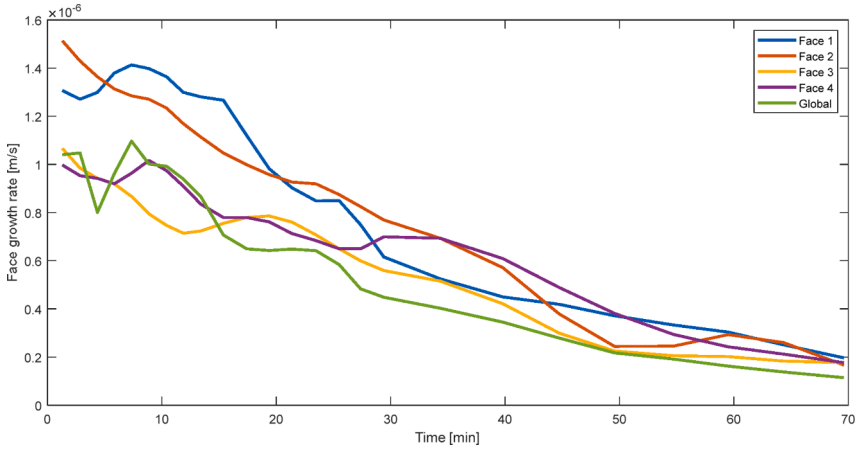

Fig. 6. Faces growth rate and crystal growth rate Eq. (1) according to time during the crystallization process.

Declaration of Competing Interest

The authors declare that they have no known competing financial interests or personal relationships that could have appeared to influence the work reported in this paper.

Data availability

Data will be made available on request.

Acknowledgement

The project leading to this publication has received funding from the IMI (Institut Mécanique et Ingénierie, Aix Marseille University).

References

[1] J.W. Mullin, Crystallization, 4th ed., Butterworth-Heinemann, Oxford; Boston, 2001.
[2] J. Bernstein, R.J. Davey, J. Henck, Concomitant Polymorphs. Angew Chem Int Ed 38 (1999) 3440–3461, https://doi.org/10.1002/(SICI)1521-3773(19991203)38:23<3440::AID-ANIE3440>3.0.CO;2-#.
[3] X.Z. Wang, K.J. Roberts, C. Ma, Crystal growth measurement using 2D and 3D imaging and the perspectives for shape control, Chem. Eng. Sci. 63 (2008) 1173–1184, https://doi.org/10.1016/j.ces.2007.07.018.
[4] T.D. Turner, P. Gajjar, I.S. Fragkopoulos, J. Carr, T.T.H. Nguyen, D. Hooper, et al., Measuring the particle packing of L -glutamic acid crystals through X-ray computed tomography for understanding powder flow and consolidation behavior, Cryst. Growth Des. 20 (2020) 4252–4263, https://doi.org/10.1021/acs.cgd.9b01515.
[5] P. Gajjar, I.D. Styliari, T.T.H. Nguyen, J. Carr, X. Chen, J.A. Elliott, et al., 3D characterisation of dry powder inhaler formulations: developing X-ray micro computed tomography approaches, Eur. J. Pharm. Biopharm. 151 (2020) 32–44, https://doi.org/10.1016/j.ejpb.2020.02.013.
[6] G. Hypolite, J. Vicente, P. Moulin, X-ray tomography crystal characterization: automatic 3D segmentation 2022, Microsc. Microanal. (2023), https://doi.org/10.1093/micmic/ozad019.
[7] C. Thiery, Tomographie à rayons X. Tech Anal (2015), https://doi.org/10.51257/a-v3-p950.
[8] H.A. Kramers, XCIII-On the theory of X-ray absorption and of the continuous X-ray spectrum, Lond. Edinb. Dublin Philos. Mag. J. Sci. 46 (1923) 836–871, https://doi.org/10.1080/14786442308565244.
[9] B.P. Flannery, H.W. Deckman, W.G. Roberge, K.L. D'Amico, Three-dimensional X-Ray microtomography, Science 237 (1987) 1439–1444, https://doi.org/10.1126/science.237.4821.1439.
[10] J. Reimann, J. Vicente, E. Brun, C. Ferrero, Y. Gan, A. Rack, X-ray tomography investigations of mono-sized sphere packing structures in cylindrical containers, Powder Technol. 318 (2017) 471–483, https://doi.org/10.1016/j.powtec.2017.05.033.
[11] F. Meyer, S. Beucher, Morphological segmentation, J. Vis. Commun. Image Represent. 1 (1990) 21–46, https://doi.org/10.1016/1047-3203(90)90014-M.
[12] L. Vincent, P. Soille, Watersheds in digital spaces: an efficient algorithm based on immersion simulations, IEEE Trans. Pattern Anal. Mach. Intell. 13 (1991) 583–598, https://doi.org/10.1109/34.87344.
[13] A.G. Shanbhag, Utilization of information measure as a means of image thresholding, CVGIP Graph. Models Image Process 56 (1994) 414–419, https://doi.org/10.1006/cgip.1994.1037.
[14] W.E. Lorensen, H.E. Cline, Marching cubes: a high resolution 3D surface construction algorithm, ACM SIGGRAPH Comput. Graph. 21 (1987) 163–169, https://doi.org/10.1145/37402.37422.
[15] J.F. Richardson, J.H. Harker, J.R. Backhurst, Chemical Engineering: Particle Technology and Separation Processes, fifth ed., Butterworth-Heinemann, Oxford (GB), 2002.
[16] S. Petlitckaia, J. Vincente, A. Poulesquen, Characterization of a geopolymer foam by X-ray tomography, Front. Chem. 9 (2021), 754355, https://doi.org/10.3389/fchem.2021.754355.
[17] B. Munch, P. Gasser, L. Holzer, R. Flatt, FIB-nanotomography of particulate systems—Part II: Particle recognition and effect of boundary truncation, J. Am. Ceram. Soc. 89 (2006) 2586–2595, https://doi.org/10.1111/j.1551-2916.2006.01121.x.
[18] C.Y. Ma, J.J. Liu, X.Z. Wang, Measurement, modelling, and closed-loop control of crystal shape distribution: literature review and future perspectives, Particuology 26 (2016) 1–18, https://doi.org/10.1016/j.partic.2015.09.014.
[19] K. Wu, C.Y. Ma, J.J. Liu, Y. Zhang, X.Z. Wang, Measurement of crystal face specific growth kinetics, Cryst. Growth Des. 16 (2016) 4855–4868, https://doi.org/10.1021/acs.cgd.6b00189.
[20] J.C. De Anda, X.Z. Wang, X. Lai, K.J. Roberts, K.H. Jennings, M.J. Wilkinson, et al., Real-time product morphology monitoring in crystallization using imaging technique, AIChE J. 51 (2005) 1406–1414, https://doi.org/10.1002/aic.10410.
[21] T. Kovačević, A. Reinhold, H. Briesen, Identifying faceted crystal shape from three-dimensional tomography data, Cryst. Growth Des. 14 (2014) 1666–1675, https://doi.org/10.1021/cg401780p.